Energy Engineering

Tech Science Press

https://doi.org/10.32604/ee.2026.072999

ARTICLE

Mechanism Analysis and Detection Methods of Voltage Fluctuation under Wide-Band Oscillation

Guofeng Zhuang[1], Xiuzhen Zhao[2], Xuemei Luo[3,*], Shibin Chen[3] and Xujun Zhang[3]

[1]State Grid Gansu Electric Power Company, Lanzhou, China
[2]State Grid Gansu Electric Power Company Extra High Voltage Branch, Lanzhou, China
[3]Electric Power Research Institute of State Grid Gansu Electric Power Company, Lanzhou, China

*Corresponding Author: Xuemei Luo. Email: 18153646889@163.com

Received: 09 September 2025; Accepted: 03 March 2026; Published: 18 June 2026

ABSTRACT: This paper investigates voltage fluctuations in direct-drive wind farms induced by wide-band oscillations during grid integration. A sequence impedance model of the wind farm is established, incorporating key components such as direct-drive wind turbines, static var generators (SVGs), transformers, and transmission lines. Based on this model, positive- and negative-sequence impedance expressions are derived. The quantitative relationship among voltage fluctuation, system strength (short-circuit ratio, SCR), and power imbalance is formulated, leading to a comprehensive expression that highlights the influence of impedance mismatch between positive and negative sequences on wide-band oscillations. Simulation results confirm an approximately linear correlation between voltage fluctuation and power imbalance, and validate the inverse relationship between voltage fluctuation and system strength. Sensitivity analysis and modal participation factor analysis are further conducted to identify the voltage response characteristics under active and reactive power disturbances, revealing that capacitor voltage, q-axis current, and phase-locked loop (PLL) states are the dominant factors driving voltage fluctuations in the wide-band frequency domain. To mitigate these effects, a frequency-weighted adaptive virtual impedance shaping (FW-AVZ) method is proposed for both positive and negative sequences. The method effectively equalizes sequence impedances, improves phase margin, and suppresses voltage fluctuations across a wide frequency range. The findings provide theoretical insights and practical guidance for enhancing voltage stability in direct-drive wind farms under weak grid conditions.

KEYWORDS: Direct-drive wind farm; wide-band oscillation; voltage fluctuation; sequential impedance modeling; power imbalance

1 Introduction

With the global transition toward clean energy, the share of renewable generation technologies, especially direct-drive wind farms, in power systems is rapidly increasing [1–3]. However, because direct-drive wind farms are connected to the grid through power electronic converters, their impedance interaction with the weak grid, the dynamic response of the phase-locked loop (PLL), and active and reactive power imbalances can induce broadband oscillations ranging from a few hertz to several kilohertz. Medium- to high-frequency oscillations exceeding several hundred hertz have been reported in Hami, Germany, Yunnan, and Zhejiang [4–6]. Broadband oscillations can lead to voltage fluctuations at the point of common coupling, unstable equipment operation, and even grid instability, posing a significant threat to the safe operation of power systems. Therefore, studying the voltage fluctuation mechanism in direct-drive wind farms under broadband oscillation and revealing the key influencing factors are of great theoretical and practical importance for ensuring grid stability [7,8].

In order to solve the resonance problem in power systems, many scholars have conducted in-depth research on the resonance mechanism of power electronic systems. Literature [9] summarizes the oscillation phenomena in modern power systems influenced by power electronic systems, describes the mechanism of broadband oscillation problems, and introduces the concept of impedance network modeling and stability criteria based on the frequency characteristics of aggregated impedance. Literature [10] discusses that resonance may occur in power systems when the system impedance is resistive and inductive and when some inverters exhibit negative conductance. Currently, There is extensive literature on the mechanisms, characteristics, and control methods for oscillations in wind farms [11–14]. Literature [15] proposes a dynamic energy model for direct-drive wind farms, which reflects the mechanism of machine-grid interactions and inter-machine interactions on the sub-synchronous oscillations by comparing the energy relationship between the motor grids at the time of sub-synchronous oscillations occurrence. The oscillation mechanism generated by wind farms is analyzed in literature [16,17], which conducts an in-depth study of sub-synchronous oscillations in direct-drive wind farms connected to AC grids, constructs a long-distance transmission impedance model for direct-drive wind farms, and analyzes the influence of factors such as grid strength, wind turbine output, and PLL control parameters on sub-synchronous oscillations. Literature [18], based on the basic principles of eigenvalue analysis, derives the theoretical calculation formula for quantitative evaluation indices of participation factors, establishes a small-signal model of an Modular Multilevel Converter-High-Voltage Direct Current (MMC-HVDC) transmission system for a wind farm, and analyzes the relationship between oscillation modes and state variables in the MMC-HVDC transmission system. Literature [19] provides an in-depth study of the detailed modeling of direct-drive wind turbines connected to a weak grid and the structural layout of each sub-module. The study carefully analyzes the functional behavior of these turbines in weak grid scenarios and provides an in-depth analysis of the interactions between direct-drive wind turbines and weak grids. Literature [20] proposes an energy compensation-based method for the suppression of sub/super synchronous oscillations in direct-drive wind turbines. It is verified that the method can achieve fast frequency-dependent suppression of sub/hyper-synchronous oscillations in different frequency bands under different grid strengths. Literature [21] presents the model construction and stability analysis of wind farms and transmission systems. Through in-depth oscillation analysis, combined with practical cases, it is shown that strategically optimized control and unprotection strategies can effectively reduce the oscillation risk of wind farms accessed through the Voltage Sourced Converter-High Voltage Direct Current (VSC-HVDC) system, thus ensuring their safe and stable operation.

However, the current research on the analysis and mechanism of wide-band oscillation of direct-drive wind farms connected to the AC power grid is not comprehensive enough. When direct-drive wind farms are connected to the grid through power electronic converters, their complex interactions with the grid may trigger wide-band oscillation, leading to fluctuations in the voltage at the grid point, which in turn affects the stability of the grid. System power imbalance also causes different degrees of wide-band oscillations, and these problems are not well analyzed at this stage. Aiming at the above problems, this paper proposes a method to analyze the voltage fluctuation mechanism of direct-drive wind farms under wide-band oscillation based on sequential impedance modeling. Firstly, the positive and negative sequence impedance models of direct-drive wind turbines, SVG, transformers and transmission lines are established by the harmonic linearization method, and the equivalent impedance expressions of direct-drive wind farms are deduced. Secondly, based on the model, the relationship between system voltage and system strength (SCR), active and reactive power inequality is quantitatively analyzed, and the comprehensive voltage fluctuation expression is derived, which reveals the influence mechanism of the positive and negative sequence impedance difference on the wide-band oscillation. Finally, sensitivity analysis and modal factor analysis are used to identify the key factors triggering voltage fluctuations, and the accuracy of the derived equations and the influence law of system strength on oscillations are verified through simulation. The research in this paper provides theoretical basis and engineering guidance for the suppression of wide-band oscillations in direct-drive wind farms and the stable operation of power grids. The main contributions and novelty of this paper are summarized as follows:

1. A method for analyzing the voltage fluctuation mechanism in direct-drive wind farms under broadband oscillation is proposed based on sequential impedance modeling. It integrates the impedance characteristics of wind turbines, SVGs, transformers, and transmission lines into a unified analytical framework.
2. A quantitative relationship between voltage fluctuation, system strength, and power imbalance is established. An explicit, comprehensive voltage fluctuation expression is derived, which reveals the critical impact of positive- and negative-sequence impedance mismatch on broadband oscillation amplification.
3. Through sensitivity and modal participation factor analyses, the key driving factors of voltage fluctuations in the broadband frequency domain are identified. It is shown that voltage sensitivity is dominant in low frequencies and decays exponentially with frequency, while capacitor voltage and PLL states are the most participative state variables.
4. A Frequency-Weighted Adaptive Virtual Impedance Shaping method is proposed and validated. This method aims to equalize positive- and negative-sequence impedances, enhance phase margin, and suppress voltage fluctuations across a wide frequency band.

2 Impedance Modeling of Direct-Drive Wind Farms under Wide-Band Oscillation

2.1 Direct-Drive Turbine Sequence Impedance Modeling

With the wide application of new energy, the proportion of direct-drive wind farms in the power system is gradually increasing. However, when direct-drive wind farms are connected to the power grid, problems such as wide-band oscillation occur frequently, which seriously affect the safe and stable operation of the power grid. Establishing an accurate impedance model of direct-drive wind farms helps to deeply analyze the mechanism of these problems and propose effective solution measures. In actual operation, the power imbalance phenomenon is widespread, which has an important impact on the voltage characteristics of wind farm equipment, so the derivation of the voltage expression by considering the power imbalance factor can make the established model more accurately reflect the operation status of direct-drive wind farms.

Fig. 1 shows the topology of the direct-drive wind power structure. Where i_a, i_b, i_c is the output current of the grid side inverter and $v_a, \mathrm{v}_b, \mathrm{v}_c$ is the output voltage of the grid side inverter. Where the grid side inverter is connected to the transmission line through a transformer (0.69/35 kV) and a filter.

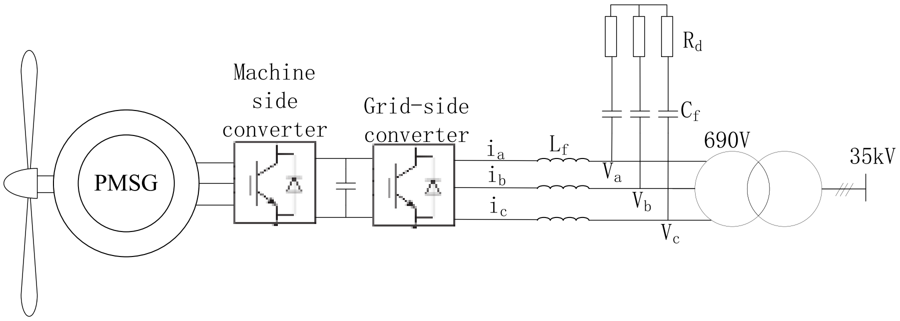

Figure 1: Direct-drive wind power structure topology.

Direct-drive wind turbines are mainly composed of permanent magnet synchronous generators (PMGs), power electronic power converters (PECs), and filtering links. The permanent magnet synchronous generator (PMG) converts wind energy into electrical energy, which is connected to the grid through a back-to-back power electronic converter. The machine-side converter adopts constant DC-side voltage control, and the grid-side converter adopts constant power or constant current output control. The direct-drive wind turbine grid-connected inverter adopts double closed-loop control with voltage outer loop and current inner loop and phase-locked loop control in dq coordinate system to ensure synchronous operation with the grid.

Current inner loop controller $H_i\left(s\right)$ and phase-locked loop controller $H_{PLL}\left(s\right)$, respectively:

$$H_i\left(s\right) = k_{p\_i} + \frac{k_{i-i}}{s} \tag{1}$$

$$H_{PLL}\left(s\right) = \frac{\left(k_{p\_P} + \frac{k_{i\_p}}{s}\right)}{s} \tag{2}$$

where k_{p-i}, k_{i-i} is the current loop PI control parameter and k_{p-P}, k_{i-P} is the phase-locked loop PI controller parameter.

A harmonic linearization method is utilized to inject positive and negative sequence small-signal harmonic voltage sources between the direct-drive wind turbine grid-connected converter and the grid. Based on the Fourier transform and convolution theorem, the time-domain AC quantities are transformed into frequency-domain direct flow quantities to achieve nonlinear partial linearization. It is assumed that the phase A voltage-current expression is:

$$v_a\left(t\right) = V_1\cos\left(\omega_1 t\right) + V_p\cos\left(\omega_p t + \varphi_{vp}\right) + V_n\cos\left(\omega_n t + \varphi_{vn}\right) \tag{3}$$

$$i_a\left(t\right) = I_1\cos\left(\omega_1 t + \varphi_{i1}\right) + I_p\cos\left(\omega_p t + \varphi_{ip}\right) + I_n\cos\left(\omega_n t + \varphi_{in}\right) \tag{4}$$

Considering the effect of phase-locked loop for park transformation, the positive and negative sequence impedance model of direct-drive wind turbine generator is obtained as:

$$Z_{PMSG,p}\left(s\right) = -\frac{V_p}{I_p} = \frac{sL_{f1} + \frac{V_{dc}}{2}\left[H_i\left(s - j2\pi f_1\right) - jK_1\right]}{1 - \frac{V_{dc}}{2}K_f - \frac{V_dC}{4}F_{PLL}\left(s - j2\pi f_1\right)H_i\left(s - j2\pi f_1\right)\left(I_{dref} + jI_{dref}\right)} \tag{5}$$

$$Z_{PMSG,n}\left(s\right) = -\frac{V_n}{I_n} = \frac{sL_{f1} + \frac{V_{dc}}{2}\left[H_i\left(s + j2\pi f_1\right) + jK_1\right]}{1 - \frac{V_{dc}}{2}K_2 - \frac{V_{dc}}{4}F_{PLL}\left(s + j2\pi f_1\right)H_i\left(s + j2\pi f_1\right)\left(I_{dref} - jI_{dref}\right)} \tag{6}$$

where L_{f1} is the filter inductance, V_{dc} is the DC side voltage, K_1, K_2 are the control coefficients, and $F_{PLL}\left(s\right)$ is the phase-locked loop closed-loop transfer function.

2.2 Sequential Impedance Modeling of Stationary Reactive Generator (SVG)

In direct-drive wind farms, SVGs are used for *in situ* reactive power compensation to improve system transmission efficiency. The voltage-type SVG studied in this paper adopts a constant reactive power control mode with double closed-loop control of power outer loop and current inner loop. The reactive power outer loop and current inner loop expressions are, respectively:

$$i_{qref} = -H_Q\left(s\right)\left(Q_{ref} - Q\right) \tag{7}$$

$$\begin{cases} u_{ds} = \left(i_{dref} - i_d\right)H_i\left(s\right) - K_{d2}i_q \\ u_{qs} = \left(i_{qref} - i_q\right)H_i\left(s\right) + K_{d2}i_d \end{cases} \tag{8}$$

where, $H_i\left(s\right)$ is the current inner loop transfer function, K_{d2} is the current feed-forward coefficient and $H_Q\left(s\right)$ is the reactive outer loop transfer function.

A small disturbance voltage signal is added to the output of SVG, then the A-phase voltage-current of SVG in stationary coordinate system is:

$$\begin{aligned} v_{aSVG}\left(t\right) = {} & V_1\cos\left(\omega_1 t\right) + V_{\mathrm{p}}\cos\left(\omega_{\mathrm{p}}t + \varphi_{\mathrm{vp}}\right) \\ & + V_{\mathrm{n}}\cos\left(\omega_{\mathrm{n}}t + \varphi_{\mathrm{vn}}\right) \end{aligned} \tag{9}$$

$$\begin{aligned} i_{aSVG}\left(t\right) = {} & I_1\cos\left(\omega_1 t + \varphi_{\mathrm{i}1}\right) + I_{\mathrm{p}}\cos\left(\omega_{\mathrm{p}}t + \varphi_{\mathrm{ip}}\right) \\ & + I_{\mathrm{n}}\cos\left(\omega_{\mathrm{n}}t + \varphi_{\mathrm{in}}\right) \end{aligned} \tag{10}$$

Same as the direct-drive turbine sequence impedance modeling, the SVG output equivalent impedance model is obtained by simplifying Eqs. (9) and (10) taking into account the phase-locked loop effect:

$$\begin{aligned} Z_{\mathrm{SVG,p}}\left(s\right) = -\frac{V_p}{I_p} = {} & \frac{sL_f+}{1 + \frac{V_{dc}}{4}F_{\mathrm{PLL}}\left(s - j2\pi f_1\right)} \\ & \frac{\frac{V_{dc}}{2}\left[H_i\left(s - j2\pi f_1\right) - jK_{d2}\right]}{\dfrac{\begin{matrix} H_i\left(s - j2\pi f_1\right)\left[I_{def} + jQ_{ref}H_Q\left(s - j2\pi f_1\right)\right] \\ +\frac{3}{8}V_{dc}H_i\left(s - j2\pi f_1\right)H_Q\left(s - j2\pi f_1\right)V_1 \end{matrix}}{-j\frac{3}{8}V_{dc}H_i\left(s - j2\pi f_1\right)H_Q\left(s - j2\pi f_1\right)I_1}} \end{aligned} \tag{11}$$

$$\begin{aligned} Z_{\mathrm{SVG,n}}\left(s\right) = -\frac{V_n}{I_n} = {} & \frac{sL_f+}{1 + \frac{V_{dc}}{4}F_{\mathrm{PLL}}\left(s + j2\pi f_1\right)} \\ & \frac{\frac{V_{\mathrm{dc}}}{2}\left[H_i\left(s + j2\pi f_1\right) + jK_{d2}\right]}{\dfrac{\begin{matrix} H_i\left(s + j2\pi f_1\right)\left[I_{dref} - jQ_{ref}H_Q\left(s + j2\pi f_1\right)\right] \\ +\frac{3}{8}V_{\mathrm{dc}}H_i\left(s - j2\pi f_1\right)_1 H_Q\left(s - j2\pi f_1\right)V \end{matrix}}{+j\frac{3}{8}V_{dc}H_i\left(s + j2\pi f_1\right)H_Q\left(s + j2\pi f_1\right)I_1}} \end{aligned} \tag{12}$$

2.3 Transformer and Transmission Line Sequence Impedance Modeling

In direct-drive wind farms, the output of the direct-drive turbine is connected to the bus through a transformer, and the transformer is modeled by a T-equivalent circuit with the impedance parameter expression:

$$\begin{cases} Z_{T1} = R_{T1} + jX_{T1} \\ Z_{T2} = \left(\dfrac{N_1}{N_2}\right)^2 R_{T2} + j\left(\dfrac{N_1}{N_2}\right)^2 (X_{T2}) \\ Z_{Tm} = jX_{Tm} \end{cases} \tag{13}$$

where, R_{T1}, X_{T1} is the resistance and reactance of the primary side, respectively, the secondary side is R_{T2}, X_{T2}, the excitation reactance is X_{Tm}, and N is the turns ratio.

Considering the long distance of each generating equipment in the wind farm, the transmission line impedance cannot be neglected. Adopting the lumped parameter model, the equivalent impedance and equivalent conductance of the π-type equivalent circuit are expressed as follows:

$$\begin{cases} Z_L = r_0 l + jx_0 l \\ Y_L = j\dfrac{1}{2} b_0 l \end{cases} \tag{14}$$

where l is the length of the transmission line, and r_0, x_0, b_0 is the resistive reactance and conductance per unit length of the transmission line, respectively.

2.4 Sequential Impedance Modeling of Direct-Drive Wind Farms

The simplified equivalent circuit diagram of the direct-drive wind farm is shown in Fig. 2:

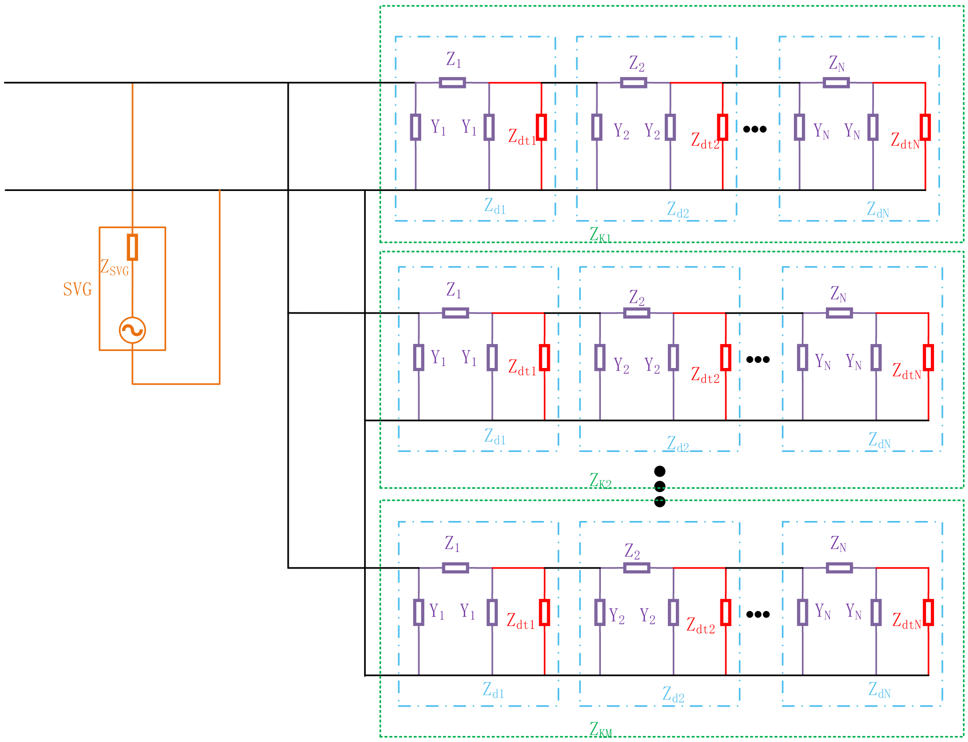

Figure 2: Simplified equivalent circuit of a direct-drive wind farm.

In a wind farm which usually includes multiple direct-drive turbines, the overall wind farm is modeled with sequential impedance, and the equivalent impedance expression of the direct-drive wind farm is obtained through the circuit principle as:

$$Z_{eq} = \frac{1}{\frac{1}{Z_{SVG}} + \frac{1}{Z_{k1}} + \frac{1}{Z_{k2}} + \cdots + \frac{1}{Z_{km}}} \tag{15}$$

The transformer equivalent impedance is set to:

$$Z_{\mathrm{dtN}} = Z_{\mathrm{T2}} + \frac{1}{\frac{1}{Z_{\mathrm{Tm}}} + \frac{1}{k_{\mathrm{dt}}^2 Z_{\mathrm{PMSG}} + Z_{\mathrm{T1}}}}, N = 1, 2, 3, \cdots \tag{16}$$

The transmission line equivalent impedance expression is:

$$Z_{\mathrm{dN}} = \frac{1}{Y_{\mathrm{N}} + \frac{1}{Z_{\mathrm{N}}} + \frac{1}{Y_{\mathrm{N}}} \| Z_{\mathrm{dtN}}}, N = 1, 2, 3, \cdots \tag{17}$$

Bringing Eqs. (16) and (17) into Eq. (15), the positive and negative sequence impedance expression for direct-drive wind farm is obtained as:

$$Z_{\mathrm{eq,p}}(s) = Z_{\mathrm{SVG,p}}(s) \parallel \frac{1}{m\{Y_1 + \frac{1}{\frac{1}{Z_1} + \frac{1}{Y_1} \| Z_{\mathrm{Tm}} \| \left(k_{dt}{}^2 Z_{\mathrm{PMSG,p}}(s) + Z_{\mathrm{I}}\right) + Z_{\mathrm{T2}}] \| Z_{\mathrm{dL2}}}\}} \tag{18}$$

$$Z_{\mathrm{eq,n}}(s) = Z_{\mathrm{SVG,n}}(s) \parallel \frac{1}{m\{Y_1 + \frac{1}{\frac{1}{Z_1 + Y_1} \| Z_{\mathrm{Tm}} \| (k_{dt}{}^2 Z_{\mathrm{PMSG,n}}(s) + Z_{\mathrm{I}}) + Z_{\mathrm{T2}}] \| Z_{\mathrm{dL2}}}\}} \tag{19}$$

3 Voltage Fluctuations under Wide-Band Oscillations in Direct-Drive Wind Farms

In the grid-connected operation of direct-drive wind farms, wide-band oscillations (100 Hz to several kHz) are frequent and threaten the grid stability due to converter-weak grid impedance interaction, phase-locked loop (PLL) dynamics, and power imbalance. In this section, based on the model in the previous section, the integrated voltage fluctuation expressions for active and reactive power imbalance are derived to reveal the effect of positive and negative sequence impedance differences on wide-band oscillations.

The system strength is generally quantified by the short-circuit capacity ratio (SCR) of the system, where the short-circuit ratio expression is shown in Eq. (20):

$$\mathrm{SCR} = \frac{S_{SC}}{S_N} = \frac{V^2{}_{PCC}}{Z_{grid} \cdot S_N} \tag{20}$$

where S_{SC} is the grid short circuit capacity and $S_N = \sqrt{P_N^2 + Q_N^2}$ is the rated power. V_{PCC} is the rated voltage at the grid connection point. Z_{grid} is the equivalent impedance of the power grid.

3.1 Effect of Active Unevenness on Voltage

The active power is based on the three-phase system expression:

$$P = \frac{3}{2} V_d i_d \approx V_1 i_d \tag{21}$$

Therefore the current deviation is:

$$\Delta i_d = \frac{\Delta P}{V_1} \tag{22}$$

where ΔP is the active inequality measure. $\Delta P = P - P_{ref}$.

Since $H_i(s) = \frac{\Delta u_d}{\Delta i_{\mathrm{dref}} - \Delta i_d}$ is brought into Eq. (1) and assuming $\Delta i_{\mathrm{dref}} = 0$ at steady state, the voltage deviation ΔV_d is satisfied:

$$\Delta V_d = -H_i(s)\,\Delta i_d = -\left(k_{p-i} + \frac{k_{i-i}}{s}\right)\Delta i_d \tag{23}$$

can be obtained by ignoring the dynamic process:

$$\Delta V_d \approx -\frac{k_{i-i}}{k_{p-i}}\Delta i_d = -\frac{k_{i-i}}{k_{p-i}V_1}\Delta P \tag{24}$$

From this it follows that ΔV_d is approximately proportional to ΔP, proportional to k_{i-i} and inversely proportional to k_{p-i}.

3.2 Effect of Reactive Power Inequality on Voltage

The SVG reactive power control expression is shown in Eq. (7), where the reactive power inequality measures $\Delta Q = Q_{\mathrm{ref}} - Q$, then $\Delta i_q = -H_Q(s)\,\Delta Q$. The PLL regulates the phase through the q-axis voltage deviation and the expression is written as:

$$\Delta\theta = H_{PLL}(s)\,\Delta V_q \tag{25}$$

where $H_{PLL}(s)$ is the same as Eq. (2).

The voltage coupling due to phase deviation is:

$$\Delta V_d \approx -V_1\Delta\theta,\ \Delta V_q \approx V_1\Delta\theta. \tag{26}$$

The voltage of the q-axis is:

$$\Delta V_q = \Delta u_q - sL_f\Delta i_q + V_1\Delta\theta \tag{27}$$

The Eqs. (23) and (25) can be obtained by bringing them into Eq. (27):

$$\Delta V_q = -\left(k_{p-i} + \frac{k_{i-i}}{s} + sL_f\right)\Delta i_q + V_1 H_{PLL}(s)\,\Delta V_q \tag{28}$$

From there, it can be obtained:

$$\Delta V_q\left[1 - V_1 H_{PLL}(s)\right] = -\left(k_{p-i} + \frac{k_{i-i}}{s} + sL_f\right)\Delta i_q \tag{29}$$

Since the three-phase reactive power is $Q = \frac{3}{2}V_d i_q \approx V_1 i_q$, the amount of reactive power inequality is $\Delta Q = V_1\Delta i_q$, thus the equation between current deviation and reactive power deviation is obtained as:

$$\Delta i_q = \frac{\Delta Q}{V_1} \tag{30}$$

Substituting Eq. (29) into Eq. (30) yields:

$$\Delta V_q = -\frac{\left(k_{p-i} + \frac{k_{i-i}}{s} + sL_f\right)\frac{\Delta Q}{V_1}}{1 - V_1 \cdot \frac{k_{p-P}s + k_{i-P}}{s}} \tag{31}$$

3.3 Combined Voltage Fluctuation Expression

The positive and negative sequence voltage variations are based on the sequence impedance Eqs. (18) and (19):

$$\Delta V_p = Z_{PMSG,p}\left(s\right)\Delta I_p, \quad \Delta V_n = Z_{PMSG,n}\left(s\right)\Delta I_n \tag{32}$$

The power perturbation is:

$$\Delta I_p = \frac{\Delta S_p}{{V_P}^*} = \frac{\Delta P + j\Delta Q}{V_1}, \quad \Delta I_n = \frac{\Delta S_n}{{V_n}^*} \tag{33}$$

Among others, $\Delta S_p = \Delta P + j\Delta Q$, $\Delta S_n = \Delta P - j\Delta Q$, $|\Delta Q| < 0.1Q_N$.

The total voltage fluctuation amplitude is then:

$$|\Delta V_{PCC}| = \sqrt{|\Delta V_p|^2 + |\Delta V_n|^2} \tag{34}$$

Substituting Eqs. (32) and (33) into Eq. (34) yields:

$$\begin{gathered} \Delta V_p = Z_{PMSG,p}\left(s\right) \cdot \frac{\Delta P + j\Delta Q}{V_1}, \\ \Delta V_n = Z_{PMSG,n}\left(s\right) \cdot \frac{\Delta P - j\Delta Q}{V_1} \end{gathered} \tag{35}$$

Assuming the power imbalance ratio $\gamma = \frac{\Delta Q}{\Delta P}$, we get:

$$\begin{gathered} \Delta V_p| = |Z_{PMSG,p}\left(s\right)| \cdot \frac{|\Delta P|\sqrt{1+\gamma^2}}{V_1}, \\ |\Delta V_n| = |Z_{PMSG,n}\left(s\right)| \cdot \frac{|\Delta P|\sqrt{1+\gamma^2}}{V_1} \end{gathered} \tag{36}$$

Then the relationship between voltage fluctuation and unbalanced power is:

$$|\Delta V_{PCC}| = \frac{|\Delta P|\sqrt{1+\gamma^2}}{V_1}\sqrt{|Z_{PMSG,p}\left(s\right)|^2 + |Z_{PMSG,n}\left(s\right)|^2} \tag{37}$$

It can be seen that the relationship between the voltage fluctuation ΔV_{PCC} and the power inequality measure ΔP should be approximately linear. $|\Delta P| < 0.1P_N$, $f < 500HZ$, $|V_{PCC} - V_1| < 0.05V_1$. It should be noted that Eq. (37) is derived under several assumptions. First, the relationship between ΔV and ΔP is obtained from a small-signal linearization around a steady-state operating point, assuming that the active and reactive power imbalance ratios are sufficiently small. Second, the derivation neglects fast electromagnetic transients and higher-order nonlinearities, and is therefore valid in a quasi-steady frequency range below the dominant bandwidths of the current control loop and the PLL, typically covering the low- to mid-frequency region of the broadband oscillation spectrum. Third, the grid strength is characterized by the short-circuit ratio (SCR), and the linear approximation is most accurate under weak to moderate grid conditions, where voltage fluctuations are mainly governed by impedance interaction rather than voltage regulation saturation. Finally, the operating point is assumed to be close to rated voltage and nominal frequency. Within these conditions, Eq. (37) provides an effective analytical approximation of the voltage fluctuation caused by power imbalance.

According to Eqs. (37) and (20) can be considered:

$$\Delta V(\omega) \approx \frac{\left|Z_{grid}(\omega)\right| + \left|Z_{farm}(\omega)\right|}{3V_1} \cdot |\Delta S| = \frac{V_{PCC}^2}{3V_1.S_N.SCR} \cdot |\Delta S| \tag{38}$$

$\Delta S = \sqrt{(\Delta P)^2 + (\Delta Q)^2}$ is the apparent power imbalance, which clearly shows the inverse relationship of SCR.

3.4 Simulation Verification

The relationship between the derived voltage-power imbalance is validated in simulation using the model of the wind farm developed in Section 2. Each electrical parameter is shown in Table 1.

Table 1: Parameters in the wind farm model.

Parameters	Numerical Value	Parameters	Numerical Value
V_{dc}	1000 V	k_{pQ}	0.000012
V_1	563 V	k_{iQ}	0.0031625
P_N	2 MW	K_{d2}	0.0027
Q_N	1 MVAr	R_{T1}	0.3675 Ω
L_f	3 mH	L_{T1}	0.076 H
C_f	180 μF	R_{T2}	0.0962 mΩ
R_f	1.5 Ω	L_{T2}	0.197 mΩ
f_s	20 kHZ	R_{Tm}	0.076 mΩ
$k_{p\text{-}i}$	0.004572	L_{Tm}	229.33 H
$k_{i\text{-}i}$	81.26987	r_0	0.132 Ω/km
$k_{P\text{-}P}$	0.39885	l_0	1.21 mH/km
$k_{i\text{-}P}$	24.7473	b_0	0. 0859 μF/km
K_1	0.0026	K_2	0.02

The relationship between voltage fluctuation and power inequality is shown in Fig. 3, from which it can be seen that the relationship between voltage fluctuation and power inequality in the simulation is approximately linear, which verifies the correctness of Eq. (37).

The error between the simulation analysis and the theoretical analysis is shown in Fig. 4, and it can be seen that the error is basically around 2.5%, which further verifies the correctness of the derived formula.

The simulation plot between voltage fluctuation and system strength (SCR) is shown in Fig. 5, from which it can be seen that the larger the system strength, the smaller the voltage fluctuation, which is in accordance with the derivation of Eq. (38).

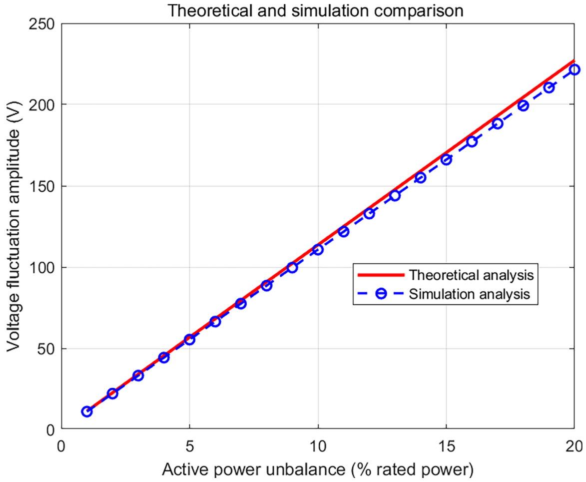

Figure 3: Relationship between voltage and power inequality measure.

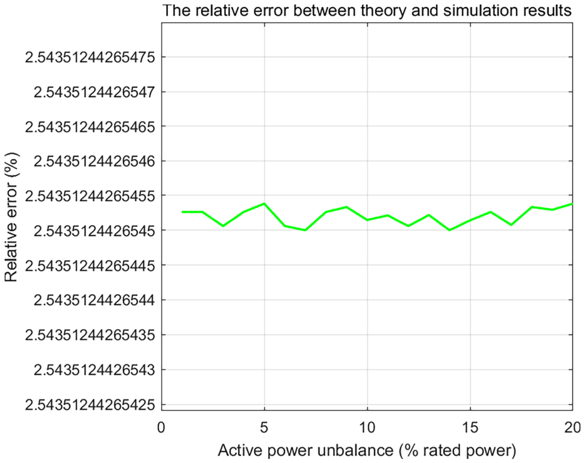

Figure 4: Relative error analysis.

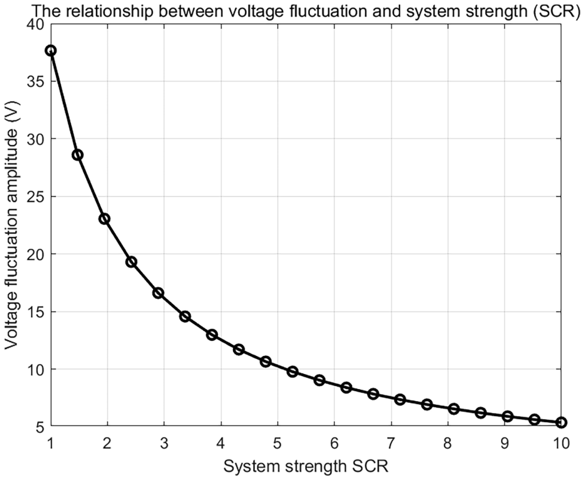

Figure 5: Relationship between system strength and voltage fluctuation.

4 Analysis of Examples

A wind power grid-connected system as shown in Fig. 2 is applied, where a direct-drive wind farm containing three transmission lines each containing five direct-drive wind turbines is constructed.

In analyzing the stability of direct-drive wind farms connected to the grid under wide-band oscillation can be used to analyze the stability of the system using the small-signal stability method, which decomposes the wind farm and the grid system into two parts, so as to analyze the stability of the system, and the system parameters and the model are used in the contents of Section 2. The simplified diagram of the grid-connected system is shown in Fig. 6.

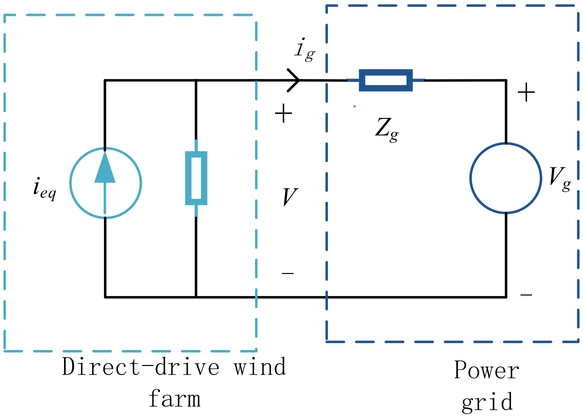

Figure 6: Simplified diagram of grid-connected system.

Where i_{eq}, Z_{eq} is the output current and equivalent impedance of the direct-drive wind farm, V_g, Z_g is the voltage and equivalent impedance of the grid side, and i_g, V is the voltage and current at the grid-connected point. According to KVL and KCL the grid-connected current can be obtained as:

$$i_g = i_{\text{eq}} \frac{Z_{\text{eq}}}{Z_{\text{eq}} + Z_{\text{g}}} - \frac{V_{\text{g}}}{Z_{\text{eq}} + Z_{\text{g}}} = \frac{1}{1 + \frac{Z_{\text{g}}}{Z_{\text{eq}}}} \left(i_{\text{eq}} - \frac{V_g}{Z_{\text{eq}}} \right) \tag{39}$$

The model is built in matlab and the voltage waveforms before and after the direct drive wind farm is connected to the grid are shown in Fig. 7. At the stage of 0–0.5 s before grid connection, the three-phase voltage waveform is relatively regular, showing a stable sinusoidal waveform, with amplitude and frequency basically remaining constant. At the 0.5 s grid-connection moment, it can be observed that the voltage waveform has obvious distortion. This is due to the fact that at the moment of grid-connection, the turbine output voltage differs from the grid voltage in amplitude, phase and frequency, resulting in a transient process when the two are connected, which triggers wide-band oscillations. After grid connection, the system after a short transition, the voltage waveform is gradually restored to a more regular sinusoidal waveform, which indicates that after grid connection, the system gradually suppresses the wide-band oscillations through its own regulation mechanism, so that the voltage tends to be stabilized.

The current waveform of the direct-drive wind farm connected to the grid is shown in Fig. 8.

In the 0–0.5 s pre-grid-connection stage, the current starts to rise gradually from 0, showing a trend similar to the rising slope, and the three-phase currents basically keep growing synchronously. At the moment of grid-connection, the current shows violent fluctuations and spikes, which is a significant reflection of wide-band oscillation in the current. After grid-connection, the current gradually stabilizes after grid-connection and fluctuates up and down around a relatively stable value.

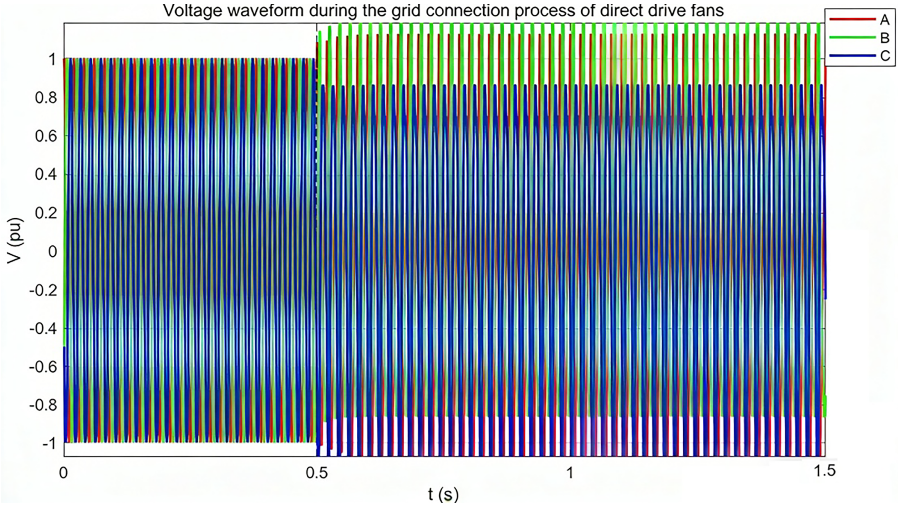

Figure 7: Voltage waveform of grid-connection process.

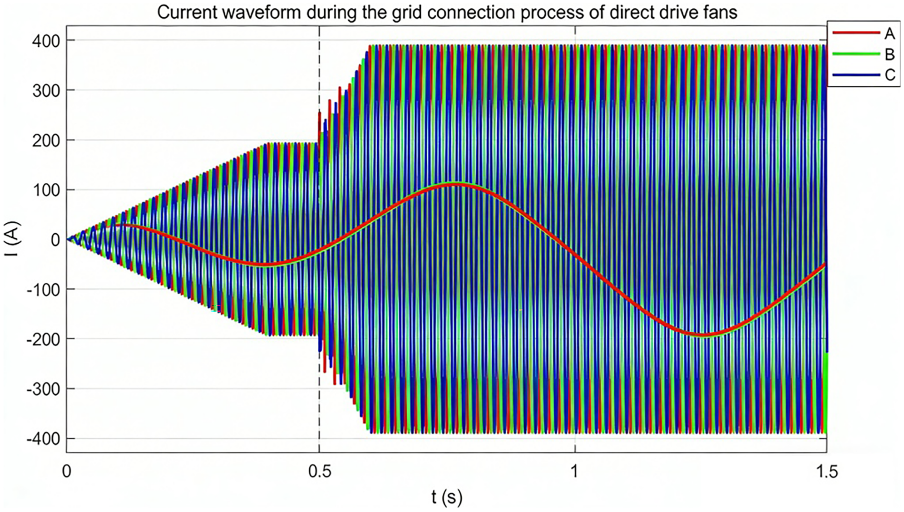

Figure 8: Current waveform of grid-connection process.

From these two figures, it can be seen that the wide-band oscillations during the grid-connection process of the direct-drive turbine are clearly reflected in the voltage and current waveforms, and they are most intense at the grid-connection instant. The wide-band oscillations of voltage and current are related to each other, and the changes of electrical parameters at the moment of grid-connection affect the stability of voltage and current at the same time.

The sensitivity of the system to voltage and active and reactive power variations using sensitivity analysis is shown in Fig. 9. The amplitude and phase responses for power balanced and unbalanced conditions are shown in the figure, which gives an indication of the frequency response pattern of the system and its sensitivity to power perturbations.

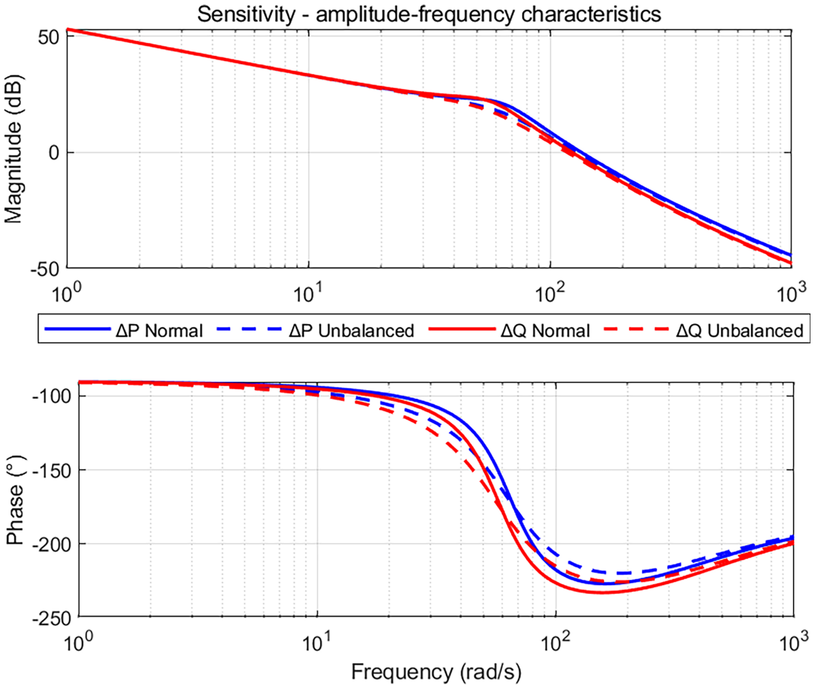

Figure 9: Voltage sensitivity to active and reactive power inequality (SCR = 1).

The sensitivity of voltage to active and reactive power inequality measures can be seen in Fig. 10, from which it can be seen that the sensitivity of voltage to the inequality measures shows an exponential decrease with the increase in frequency, which shows that the voltage is more sensitive to the perturbation of the system power in the low frequency band. The magnitude and phase of the voltage sensitivity to active and reactive power are close to the same in the figure, which indicates that the voltage response mechanism to both perturbations is similar.

When increasing the system strength it can be found that the voltage sensitivity to the active reactive power inequality measure is much closer, which indicates that the higher the system strength the lower the impact of the power inequality measure.

Voltage sensitivity to active and reactive disturbances is about 50 dB in the low frequency band and decays exponentially to −50 dB in the high frequency band. The unbalanced condition has a 5 dB higher amplitude in the low frequency band and a 10° phase advance, and the effect disappears in the high frequency band. The law reveals the low-frequency driving mechanism and high-frequency suppression characteristics of the wide-band oscillation.

A quantitative examination of Figs. 9 and 10 shows that the voltage sensitivity to active and reactive power imbalance is most pronounced in the low-frequency range. Under weak grid conditions (SCR = 1), the sensitivity reaches its maximum in the vicinity of the fundamental frequency and its neighboring band (approximately 10–50 Hz), with peak magnitudes on the order of 45–55 dB. This indicates that low-frequency power disturbances are strongly amplified and can readily induce significant voltage fluctuations. As the frequency increases, the sensitivity magnitude exhibits a clear exponential decay, decreasing to around 0 dB in the mid-frequency range (approximately 100–500 Hz) and further dropping below −40 dB in the high-frequency range above 1 kHz, implying a much weaker influence of high-frequency power disturbances on voltage variations.

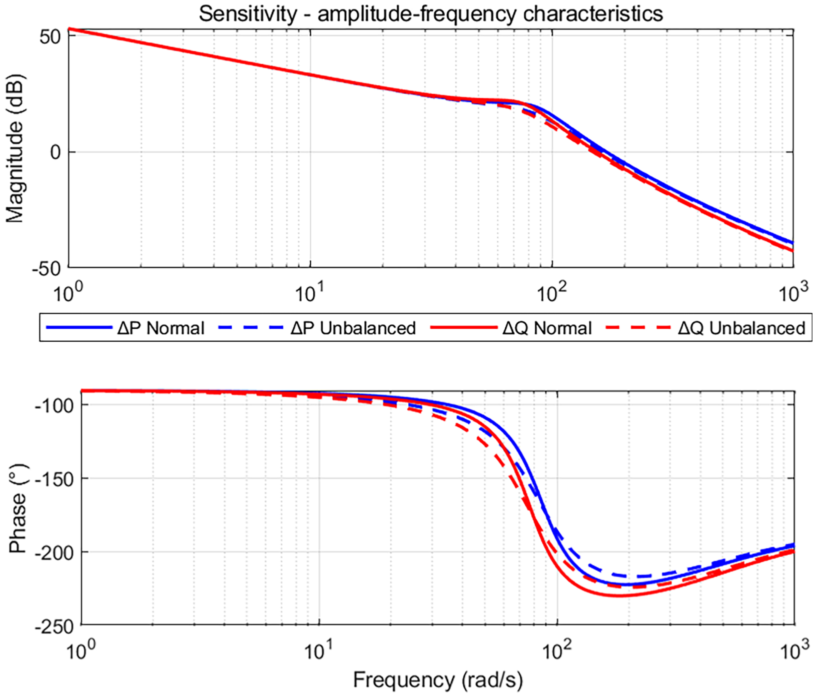

Figure 10: Voltage sensitivity to active and reactive power inequality (SCR = 2).

From a control perspective, the pronounced low-frequency sensitivity is mainly associated with the phase-locked loop (PLL) and the outer power control loop, whose bandwidths and integral gains determine the coupling strength between power perturbations and voltage response. In contrast, the sensitivity characteristics in the mid- and high-frequency ranges are dominated by the inner current control loop and the filter parameters, where the fast current regulation dynamics provide effective attenuation of power disturbances. A comparison between different grid strengths further reveals that increasing SCR (from 1 to 2) significantly reduces the low-frequency sensitivity peak, demonstrating that a stronger grid enhances voltage robustness against power imbalance disturbances.

In Figs. 11 and 12, it can be found that the unbalanced condition leads to a rightward shift of the Nyquist trajectory. It mainly affects the low-frequency range under weak grid conditions, and the low-frequency power perturbation is easily amplified under weak grid conditions, which triggers wide-band oscillations. The range of the imaginary part increases under the strong grid condition, and the strong grid suppresses the low-frequency sensitivity but amplifies the mid-frequency dynamics, indicating that the impedance-control interaction is more significant in the mid-frequency band. And it can be seen from Fig. 11 that the effect of reactive power imbalance is larger compared to active power imbalance under weak grid conditions.

In the modal participation factor analysis, only the dominant oscillatory modes relevant to broadband voltage fluctuations are considered. These modes are selected based on two criteria: a) eigenvalues located close to the imaginary axis, which have a stronger impact on system dynamic response. b) modal frequencies falling within the broadband oscillation range of interest. Modes with large damping and negligible contribution to voltage-related states are excluded. For each selected mode, participation factors are computed to identify the state variables that most strongly influence the corresponding oscillatory behavior.

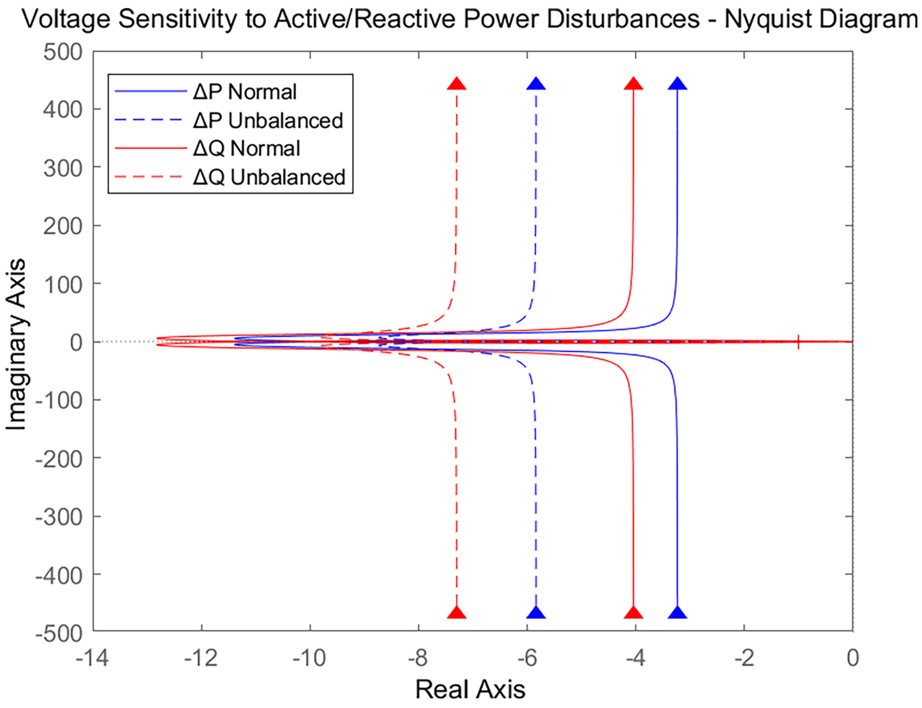

Figure 11: Nyquist diagram (SCR = 1).

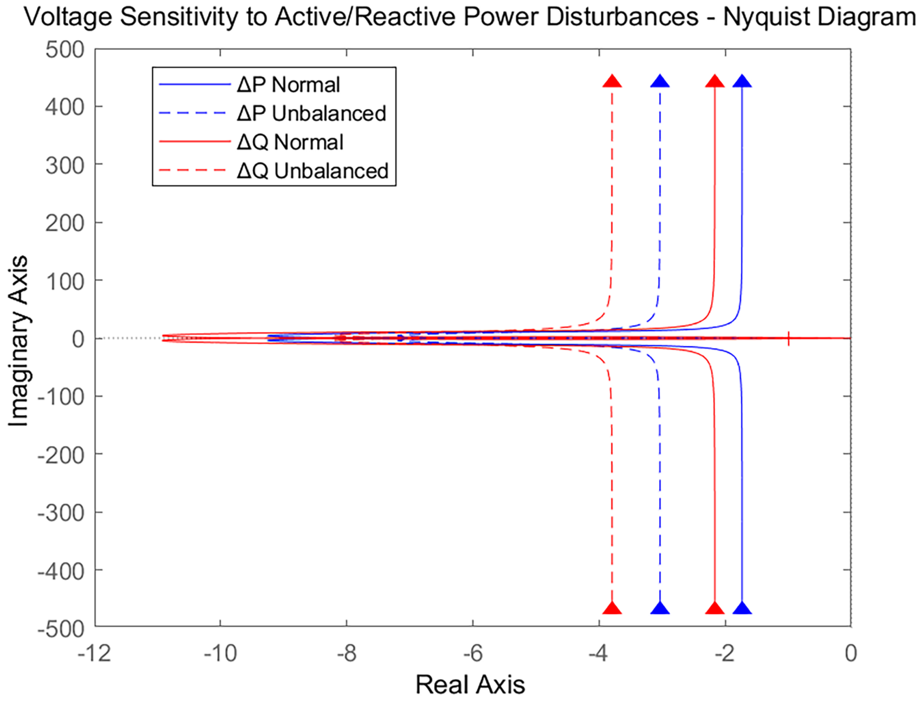

Figure 12: Nyquist diagram (SCR = 2).

In Table 2, the participation factor results indicate that broadband voltage fluctuations are primarily driven by the energy dynamics of the filter capacitor, as reflected by its consistently high participation across dominant modes. This confirms that voltage oscillations are closely linked to capacitor energy accumulation under impedance mismatch conditions. The increased participation of PLL-related states after grid connection highlights the role of phase synchronization dynamics in amplifying oscillations under weak grid conditions. Meanwhile, the current loop states contribute to shaping the oscillatory response in the mid-frequency range by regulating the converter–grid current interaction.

Table 2: Dominant modal participation factors and physical interpretation.

Dominant State Variable	Related Subsystem	Typical Participation Factor	Physical Meaning
Filter capacitor voltage v_c	LCL filter	High (0.85–0.92)	Energy storage and release in the DC/AC interface; direct manifestation of voltage fluctuation
q-axis current controller state i_q	Current inner loop	Medium–High (0.60–0.75)	Amplification or damping of oscillatory current components affecting PCC voltage
PLL phase angle θ_{PLL}	Phase-locked loop	Medium (0.30–0.45)	Coupling between grid voltage phase disturbance and converter control dynamics
Inductor current i_L	Filter inductance	Medium (0.40–0.55)	Electromagnetic energy exchange between converter and grid
Power outer-loop integrator	Power control loop	Low–Medium (0.20–0.35)	Slow power regulation affecting low-frequency voltage dynamics

In order to analyze the main factors that cause the voltage fluctuation of wide-band oscillation, the analysis method of modal participation factor is adopted, and the simulation analysis of the main participation factor before grid-connection and the main participation factor after grid-connection is carried out, which can clearly see the participation of each mode in different cases, and then analyze the main factors in wide-band oscillation, and the specific simulation diagram is shown in Fig. 13.

Establishing the modal participation factor requires considering the state variables, where the state variables for the current controller are x_{id}, x_{iq}, the state variables for the PLL are x_{pll}, the inductor current is i_{Ld}, i_{Lq}, and the capacitor voltage is v_{cd}, v_{cq}. Wide-band oscillations are triggered by high gain PLL and filter parameters. The strength of the grid system also contributes to affecting the oscillations. As can be seen from the figure, the high participation factor of v_{cd}, v_{cq} before grid connection indicates that the capacitor voltage is the main manifestation of the wide-band oscillations, which are directly associated with the voltage fluctuations. q-axis current controllers have the next highest participation factor, indicating that the current loop may amplify the oscillations. The rest of the participation factors are low, and the oscillations have less effect on these states. After grid-connection, the system strength decreases and the

v_{cd} participation factor increases, amplifying the oscillations. The participation factor of inductive current increases significantly, reflecting the enhanced current dynamics after grid-connection, and the participation factor of PLL increases, indicating that the wide-band oscillations increase the interference with phase synchronization, inducing more oscillations. Simulation results show that the wide-band oscillations trigger voltage fluctuations mainly through the high-gain PLL and filter capacitance.

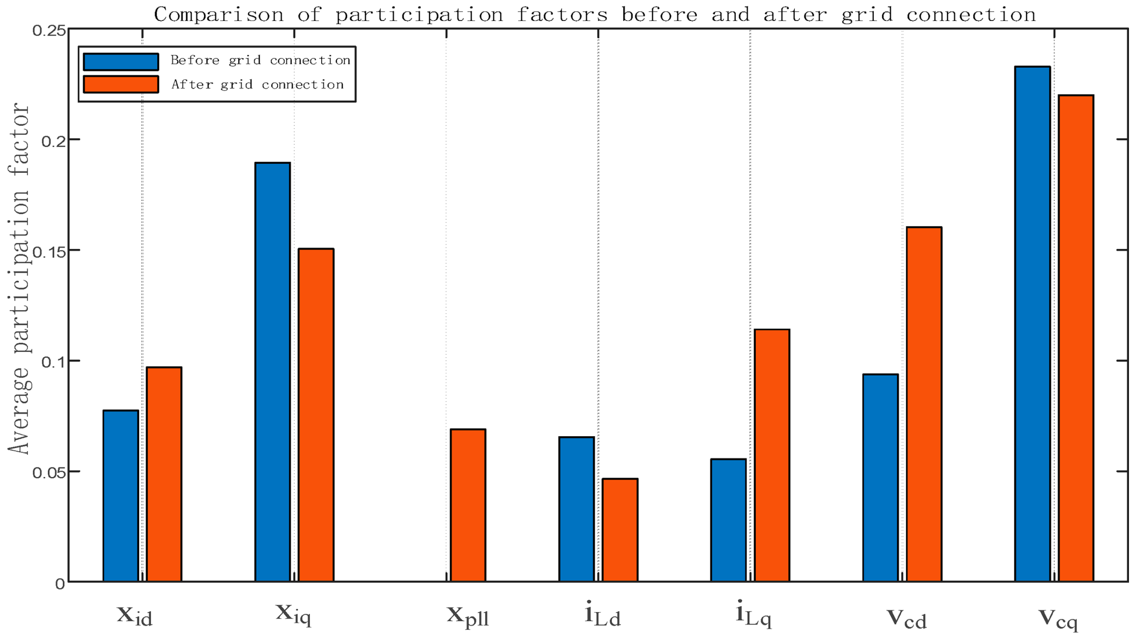

Figure 13: Modal participation factor map.

5 Frequency-Weighted Adaptive Virtual Impedance Shaping (FW-AVZ) and Validation

5.1 Methodology and Principles

To address the issue of “wide-band oscillation amplification and voltage fluctuations caused by positive/negative sequence impedance differences” revealed in the preceding section, this paper proposes a Frequency-Weighted Adaptive Virtual Impedance (FW-AVZ) [22] method. This approach introduces a frequency-weighted virtual impedance on the VSC side:

$$Z_v^{p/n}(s) = k_0 + \frac{k_1 s}{1 + s/\omega_1} + k_{\text{notch}} \frac{\omega_h s}{s^2 + 2\zeta\omega_h s + \omega_h^2}, \tag{40}$$

The low-frequency term ensures DC and low-frequency stability, the mid-frequency term provides equivalent damping and phase lead, while the notch term targets the identified oscillation center frequency ω_h Provides selective inhibition. Through optimization, it enables:

$$\min_{k_0, k_1, k_{\text{notch}}} \int_{\Omega} \left(|Z_p + Z_v^p| - |Z_n + Z_v^n|\right)^2 w(\omega)\, d\omega, \tag{41}$$

This achieves equalization of positive and negative sequence impedances while suppressing wide-band voltage fluctuations while maintaining phase margin.

This paper employs a frequency weighting function $w(\omega)$ Focus on constraining the 100 Hz–1 kHz range to achieve impedance equalization within this band. Through small-signal modeling and frequency-domain identification, real-time estimation of parameters is enabled, allowing online adjustment of FW-AVZ parameters. This method requires no additional hardware, relying solely on controller parameter tuning for implementation.

5.2 Simulation Verification

As shown in Fig. 14, without FW-AVZ, a gain peak appears near a certain frequency, indicating that power disturbances significantly affect voltage at that frequency. After implementing FW-AVZ, the gain peak decreases and the curve shape changes, demonstrating that FW-AVZ effectively reduces the impact of power disturbances on voltage and enhances voltage robustness against power disturbances.

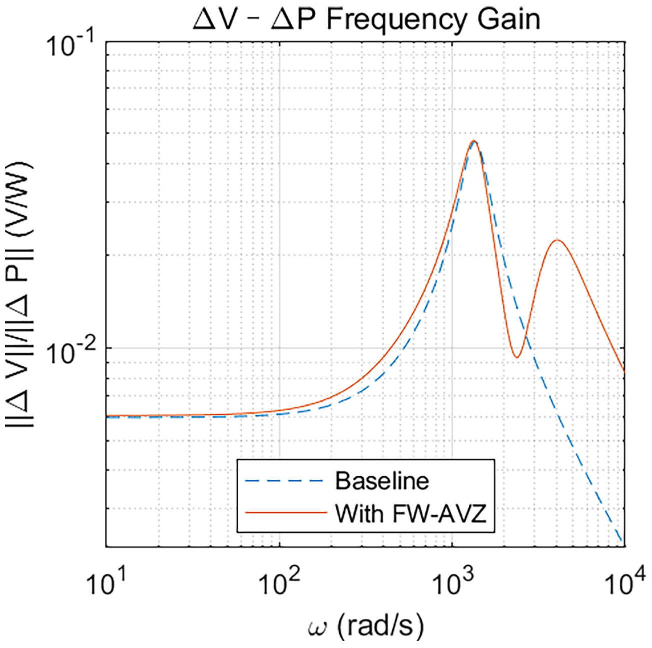

Figure 14: The frequency gain of ΔV−ΔP.

As shown in Fig. 15, SCR serves as an indicator of system strength. The figure compares the normalized voltage fluctuation metric against SCR variations under both non-FW-AVZ and FW-AVZ conditions. When FW-AVZ is implemented, the voltage fluctuation metric improves at the same SCR level, demonstrating that FW-AVZ enhances voltage stability across varying system strengths and strengthens the system's ability to suppress voltage fluctuations.

To further verify the robustness of the FW-AVZ method under varying operating conditions, additional frequency-domain sensitivity and disturbance-response simulations are conducted considering multiple grid strengths and operating points in Figs. 16–18. Simulation results indicate that under two representative grid strengths (SCR = 2 and SCR = 8) and two operating points (V1 = 500 V and V1 = 563 V), FW-AVZ is able to significantly reduce the system voltage sensitivity over a wide frequency range from 10 to 1000 Hz. In particular, in the mid-frequency band of approximately 150–300 Hz, which is commonly associated with oscillation-prone regions arising from control–grid interactions, FW-AVZ shows a strong suppression effect on sensitivity peaks.

Further disturbance-response comparisons reveal that, under different SCR and operating point conditions, FW-AVZ effectively reduces the voltage fluctuation amplitude caused by active power disturbances, with more pronounced suppression observed under weak grid conditions. These results confirm that the operating mechanism of FW-AVZ does not rely on a specific grid strength or rated operating point, demonstrating good engineering robustness and adaptability.

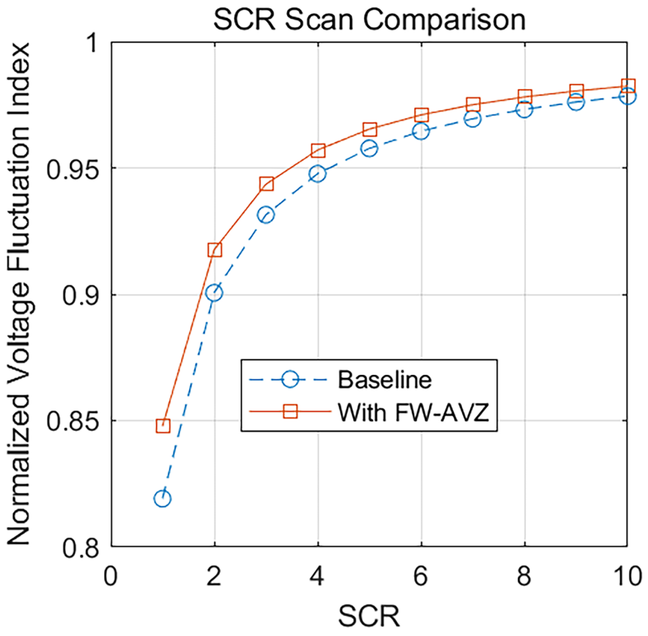

Figure 15: SCR scan comparison.

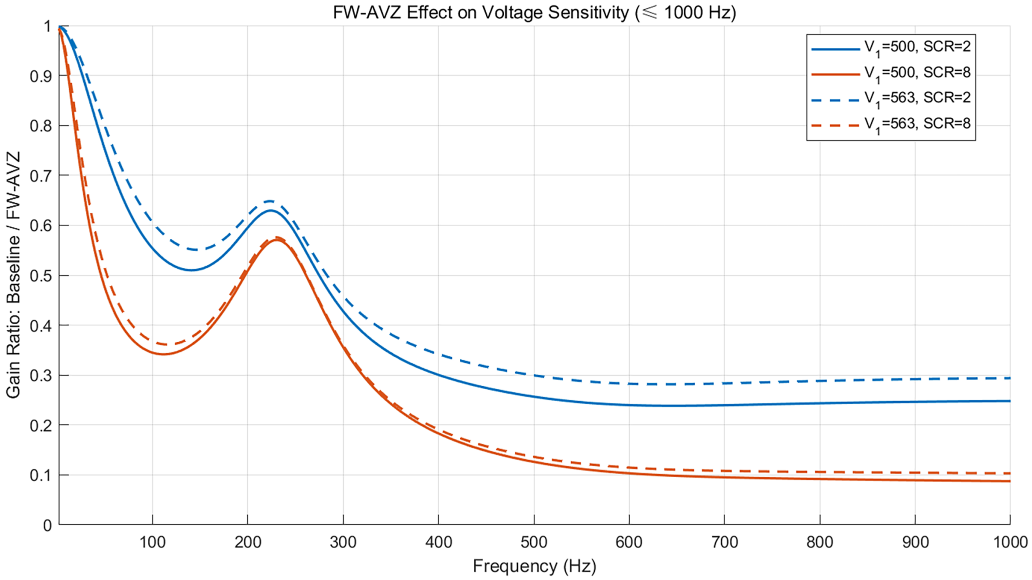

Figure 16: FW-AVZ effect on voltage sensitivity (1000 Hz).

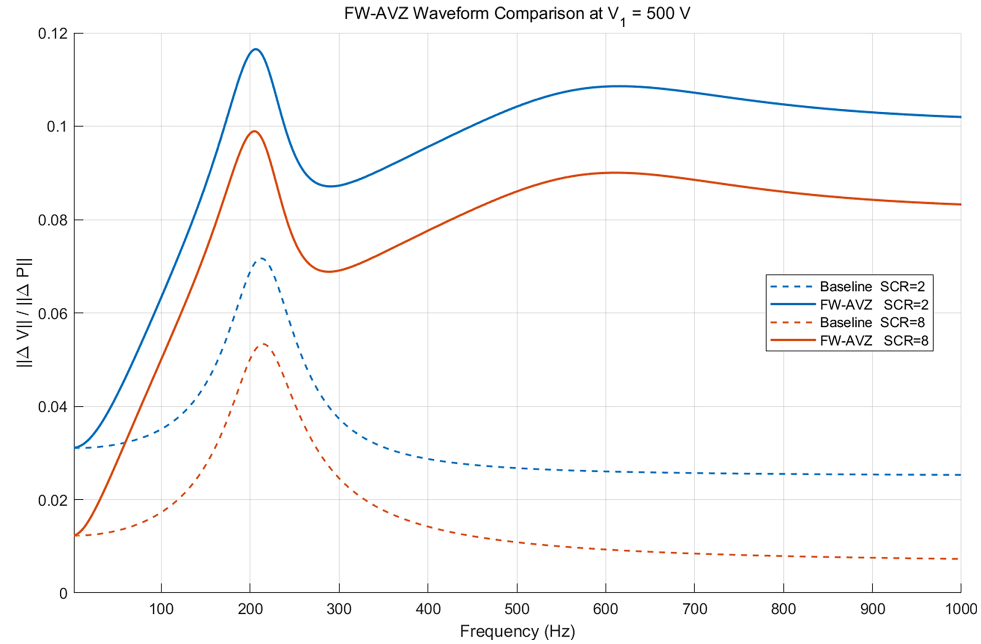

Figure 17: FW-AVZ waveform comparison at V1 = 500 V.

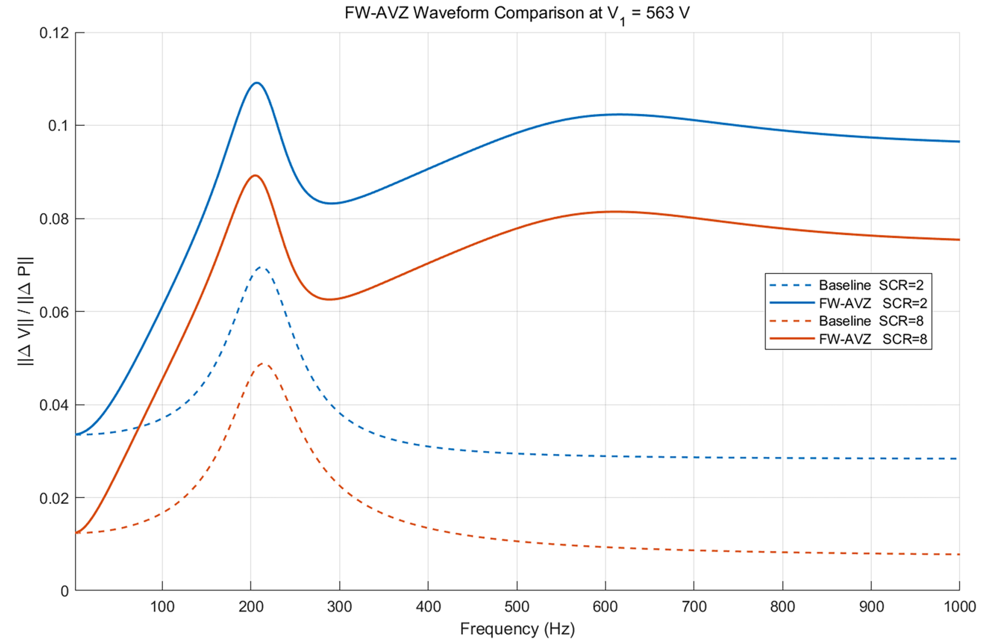

Figure 18: FW-AVZ waveform comparison at V1 = 563 V.

In summary, the FW-AVZ control strategy effectively enhances voltage stability in power systems across a wide frequency range and varying system strengths by adjusting system impedance characteristics and damping properties. This approach suppresses voltage fluctuations caused by power disturbances.

6 Conclusion

1. A comprehensive sequence impedance model incorporating key wind farm components—including wind turbines, SVGs, transformers, and transmission lines—is developed. The model accounts for essential parameters such as PI controllers, PLL dynamics, and filter characteristics, ensuring broad frequency domain applicability.
2. An approximate linear relationship between voltage deviation and power imbalance (active/reactive) is derived. The inverse correlation between voltage fluctuation and system strength (SCR) is also established and validated via simulation.
3. Sensitivity analysis shows that voltage response is most pronounced in the low-frequency domain, with peak sensitivity reaching 52.3 dB at 50 Hz, and decaying exponentially to −12.5 dB at 2.83 kHz. This indicates that broadband oscillations are driven primarily by low-frequency disturbances.
4. Modal analysis based on state-space modeling highlights that capacitor voltage, q-axis current, and PLL state variables significantly influence voltage fluctuations. After grid connection, reduced system strength amplifies oscillatory behaviors.
5. The model is based on steady-state linearization assumptions and does not fully account for nonlinear transient processes. Simulations are based on a specific wind farm configuration, requiring further experimental and field validation. Future work will focus on hardware-in-the-loop testing and extending the approach to hybrid energy systems.

Acknowledgement: None.

Funding Statement: This paper was supported by the Science and Technology Project Support of State Grid Corporation of China (No: 52272225001F).

Author Contributions: The authors confirm contribution to the paper as follows: study conception and design: Guofeng Zhuang, Xiuzhen Zhao; data collection: Xuemei Luo, Shibin Chen, Xujun Zhang; analysis and interpretation of results: Guofeng Zhuang, Xiuzhen Zhao; draft manuscript preparation: Shibin Chen, Xujun Zhang. All authors reviewed and approved the final version of the manuscript.

Availability of Data and Materials: Data supporting this study are included within the article.

Ethics Approval: Not applicable.

Conflicts of Interest: The authors declare no conflicts of interest.

References

1. Tufan K, Dalcalı A. Exploring offshore wind energy: trends, investments, and technological advancements in the global energy outlook. Russ Electr Eng. 2025;96(3):253–62. doi:10.3103/S1068371224600480.
2. Li G, Guo R, Chen J, Liu X. A single-loop active disturbance rejection control of PMSG for suppressing subsynchronous resonance. IEEE Trans Ind Electron. 2025;72(10):10233–42. doi:10.1109/tie.2025.3554956.
3. Li PH, Jia R, Cao G, Ming B, Guo Y, Wang SK, et al. A novel perspective for equivalent aggregation of wind farm: measuring the dynamic similarity between output time-series. Appl Energy. 2025;392:125958. doi:10.1016/j.apenergy.2025.125958.
4. Xiang F, Liao S, Zhang H, Luo L. Sub-synchronous oscillation phenomenon analysis of grid-connected direct drive-doubly fed hybrid wind farms via VSC-HVdc system. IEEE Access. 2025;13:37966–78. doi:10.1109/ACCESS.2025.3544685.
5. Ma NN, Xie XR, He JB, Wang H. Review of wide-band oscillation in renewable and power electronics highly integrated power systems. Proc CSEE. 2020;40(15):4720–31. (In Chinese). doi:10.1016/j.rser.2023.113148.

6. Wang Y, Zhao C, Guo C, Rehman AU. Mechanism analysis and suppression strategy of subsynchronous oscillation in VSC-HVDC connected wind farms. Int J Electr Power Energy Syst. 2025;165:110456.
7. An S, Qiu W, Pu Q, Chen S, Zheng Y, Duan J, et al. Power system wideband oscillation estimation, localization, and mitigation. IET Generation Trans Dist. 2023;17(11):2655–66. doi:10.1049/gtd2.12845.
8. Chen Y, Zhang Y, Wang Z, Liu H, Li M. Analysis and suppression of subsynchronous oscillation in PMSG-based wind farms with weak grid connection considering phase-locked loop dynamics. IEEE Trans Power Syst. 2025;40(3):3456–68. doi:10.1016/j.egyr.2024.02.009.
9. Chen L, Wang Y, Zhang H, Liu X. Wideband oscillation analysis and control in power systems with high penetration of renewable energy: a review. Renew Sustain Energy Rev. 2025;210(6):115234. doi:10.1016/j.rser.2023.113148.
10. Hou T, Jiang Y, Cai Z. Study on the resonance characteristics and active damping suppression strategies of multi-inverter grid-connected systems under weak grid conditions. Energies. 2024;17(23):5889. doi:10.3390/en17235889.
11. Du W, Wang Y, Wang H. Torsional subsynchronous oscillations caused by grid-connected wind farms in a complex multi-machine power system under the condition of near strong modal resonance. Electr Power Syst Res. 2020;179(4):106085. doi:10.1016/j.epsr.2019.106085.
12. Wang Y, Zhao C, Guo C, Rehman AU. Dynamics and small signal stability analysis of PMSG-based wind farm with an MMC-HVDC system. CSEE J Power Energy Syst. 2020;6(1):226–35. doi:10.17775/CSEEJPES.2019.02550.
13. Xie D, Lu Y, Sun J, Gu C. Small signal stability analysis for different types of PMSGs connected to the grid. Renew Energy. 2017;106:149–64. doi:10.1016/j.renene.2017.01.021.
14. Shao B, Zhao S, Gao B, Yang Y, Blaabjerg F. Adequacy of the single-generator equivalent model for stability analysis in wind farms with VSC-HVDC systems. IEEE Trans Energy Convers. 2021;36(2):907–18. doi:10.1109/TEC.2020.3028546.
15. Ma J, Xu H. Study on dynamic energy model and subsynchronous oscillation mechanism for direct-drive wind farm considering the interaction between generators. CSEE J Power Energy Syst. 2024. doi:10.17775/CSEEJPES.2022.06750.
16. Li Y, Fan L, Miao Z. Wind in weak grids: low-frequency oscillations, subsynchronous oscillations, and torsional interactions. IEEE Trans Power Syst. 2020;35(1):109–18. doi:10.1109/TPWRS.2019.2924412.
17. Shao B, Zhao S, Yang Y, Gao B, Blaabjerg F. Sub-synchronous oscillation characteristics and analysis of direct-drive wind farms with VSC-HVDC systems. IEEE Trans Sustain Energy. 2021;12(2):1127–40. doi:10.1109/TSTE.2020.3035203.
18. Qiu P, Song J, Chen Q, Zhou W, Xiong B, Tang A. Research on oscillation characteristics of wind farm sending system based on participation factor. Front Energy Res. 2022;10:997782. doi:10.3389/fenrg.2022.997782.
19. Xu P, Zhao W, Li F, Li D, Qi H. Model architecture and simulation analysis of direct-drive wind turbines connected to weak power grids. In: Proceedings of the 2024 IEEE 5th International Conference on Advanced Electrical and Energy Systems (AEES); 2024 Nov 29–Dec 1; Lanzhou, China. doi:10.1109/AEES63781.2024.10872612.
20. Ma J, Zhang M, Phadke AG. Research on sub/super-synchronous oscillation suppression method for direct-drive wind turbine based on energy compensation. IET Renew Power Gener. 2021;15(11):2502–14. doi:10.1049/rpg2.12182.
21. Yang Z, Li G, Ding Y, Peng D, Zou K, Ruan L. Analysis and suppression of offshore wind power broadband oscillation based on HVDC transmission technology. Electr Eng. 2024;107:3463–81. doi:10.1007/s00202-024-02682-4.
22. Ma J, Wang H, Li Z, Liu Y. Adaptive virtual complex impedance-based power sharing control scheme for islanded microgrids. IET Smart Grid. 2025;8(3):156–70. doi:10.1049/stg2.70014.